PNAS RESEARCH ARTICLE | BIOCHEMISTRY

# Dynamics of membrane tubulation coupled with fission by a two-component module

Soumya Bhattacharyya[a] and Thomas J. Pucadyil[a,1]

Edited by James Hurley, University of California, Berkeley, CA; received January 31, 2024; accepted April 5, 2024

**Membrane tubulation coupled with fission (MTCF) is a widespread phenomenon but mechanisms for their coordination remain unclear, partly because of the lack of assays to monitor dynamics of membrane tubulation and subsequent fission. Using polymer cushioned bilayer islands, we analyze the membrane tubulator Bridging Integrator 1 (BIN1) mixed with the fission catalyst dynamin2 (Dyn2). Our results reveal this mixture to constitute a minimal two-component module that demonstrates MTCF. MTCF is an emergent property and arises because BIN1 facilitates recruitment but inhibits membrane binding of Dyn2 in a dose-dependent manner. MTCF is therefore apparent only at high Dyn2 to BIN1 ratios. Because of their mutual involvement in T-tubules biogenesis, mutations in BIN1 and Dyn2 are associated with centronuclear myopathies and our analysis links the pathology with aberrant MTCF. Together, our results establish cushioned bilayer islands as a facile template for the analysis of membrane tubulation and inform of mechanisms that coordinate MTCF.**

polymer cushions | BAR domain–containing proteins | dynamin | membrane tubulation | membrane fission

Live cell imaging has provided valuable insights into the dynamics of reactions involving membrane tubulation coupled with fission (MTCF) during muscle development, cell migration, vesicular transport, and the entry of toxins (1–7). A striking example of a regulated tubulation process is apparent during the formation of T-tubules, which are regularly spaced plasma membrane invaginations in cardiac and skeletal muscle cells. Their growth and maturation during muscle development coincides with a change in their protein composition, which allows them to become tightly associated with the sarcoplasmic reticulum and thereby facilitate synchronous excitation–contraction coupling (8, 9). The muscle-specific isoform (isoform 8) of amphiphysin 2, also called Bridging Integrator 1 (BIN1), and the ubiquitous isoform of dynamin2 (Dyn2) are critical structural components of T-tubules (10). BIN1 contains an N-BAR domain at the N terminus that bends membranes and a Src homology 3 (SH3) domain at the C terminus that interacts with the proline-rich domain (PRD) in dynamins (11, 12). The clathrin and adaptor protein 2 binding motifs are absent in BIN1. Instead, BIN1 contains a polybasic (PI) stretch of amino acids, which confers it with the enhanced ability to bind phosphoinositide lipids (10, 12). Dynamins are large multimeric GTPases known for their role in membrane fission (13, 14). Mutations in BIN1 and Dyn2 are linked to autosomal dominant and recessive forms of centronuclear myopathies (CNMs), which are a group of congenital hereditary disorders characterized by disorganized T-tubules leading to uncoordinated force generation and muscle hypotrophy (15). The relative levels of BIN1 and Dyn2 are tightly regulated during development, with an increase in BIN1 and a decrease in Dyn2 levels correlating with increased T-tubule densities in muscle cells (16). Increased expression of Dyn2 inhibits T-tubule growth during development and overexpression of Dyn2 in myoblasts leads to the fragmentation of BIN1 tubules (17, 18). Additionally, modulating Dyn2 levels rescues CNM-like defects in disease models (17, 19–22). Previous reports indicate that BIN1 negatively regulates Dyn2 functions. Thus, BIN1 inhibits dynamin's stimulated GTPase activity and reduces Dyn2's ability to vesiculate membranes (20, 23–26). From a protein design standpoint, if the sole function of BIN1 was to tubulate membranes then just the N-BAR domain and the PI stretch should have sufficed. But BIN1 contains the dynamin-interacting SH3 domain, which implies that fission of BIN1 tubules must at some point be critical for T-tubules biogenesis.

Despite the relevance of membrane tubulation in physiology, a mechanistic understanding of the function of participant proteins has largely relied on end-point analyses of tubulated liposomes. Such analyses have provided valuable information into the organization of proteins on tubulated membranes. But real-time visualization of early intermediates and their dynamics, especially when tubulation is coupled with fission, remain missing. This is because of the lack of suitable membrane templates that are amenable to

## Significance

T-tubules are regularly spaced plasma membrane invaginations in cardiac and skeletal muscle cells. Their formation is attributed to the muscle-specific isoform of the Bin1/amphiphysin/Rvs167 (BAR) domain protein amphiphysin 2 or Bridging Integrator 1 (BIN1). But BIN1 also contains a Src homology 3 (SH3) domain that recruits the fission catalyst dynamin. So why is a BIN1-coated tubule resilient to severing by dynamin? We address this by reconstituting tubulation reactions on polymer cushioned lipid bilayers. Consistent with its role as an adaptor, BIN1 recruits dynamin2 (Dyn2) but surprisingly the recruited Dyn2 fails to engage with the membrane, thus explaining why BIN1 coated tubules are resilient to dynamin-catalyzed fission. Together, our results explain how a specific BAR domain protein has evolved mechanisms that ensure tubule stability.

Author affiliations: [a]Indian Institute of Science Education and Research, Pashan, Pune 411008, Maharashtra, India

Author contributions: S.B. and T.J.P. designed research; S.B. performed research; S.B. contributed new reagents/analytic tools; S.B. and T.J.P. analyzed data; and S.B. and T.J.P. wrote the paper.

The authors declare no competing interest.

This article is a PNAS Direct Submission.



[1]To whom correspondence may be addressed. Email: pucadyil@iiserpune.ac.in.

This article contains supporting information online at https://www.pnas.org/lookup/suppl/doi:10.1073/pnas.2402180121/-/DCSupplemental.

Published May 8, 2024.

real-time visualization and monitoring of membrane tubulation. Giant unilamellar vesicles (GUVs) are a popular template but their finite reservoir deters membrane tubulation because of heightened membrane tension. Supported bilayers with excess reservoir (SUPER) templates are a workaround, but their spherical geometry, as is also the case with GUVs, renders it difficult to track early intermediates during the tubulation reaction (27). Planar supported lipid bilayers (SLBs) possess the ideal geometry, but those formed by vesicle fusion on glass are difficult to tubulate because of strong interactions between membrane lipids and the glass surface. This is evident from the dramatic tubulation seen with multilamellar membrane sheets, where the bulk of the membrane reservoir is not in contact with glass (24, 28). But the use of multilamellar membrane sheets has been restricted to visualizing late stages of membrane tubulation reactions, only after long tubules have been drawn out from the membrane reservoir.

Ingenious adaptations in the form of SLBs formed on polymer cushions have reported enhanced diffusion of membrane lipids that facilitate protein-induced membrane remodeling (29–32). Inspired by these findings, we report the utility of polyethylene glycol (PEG)-cushioned planar bilayer islands for the quantitative analysis of membrane tubulation as well as MTCF using BIN1 and Dyn2.

## Results

**Cushioned Planar Bilayer Islands as Pliable Templates for Membrane Tubulation.** Based on previous work from our lab and others, a facile route to forming PEG-cushioned membrane templates is by spreading lipids in an organic solvent as a thin film on a glass coverslip covalently attached to PEG (*SI Appendix*, Fig. S1*A*). Drying off the solvent and subsequent hydration converts the lipid film into large planar bilayer islands (*SI Appendix*, Fig. S1*B*) (29, 33, 34). The vast expanse of the planar bilayer sometimes displays membrane buds and nanotubes, which appear brighter than the underlying bilayer because of the higher membrane area in the optical path (*SI Appendix*, Fig. S1*B*). Since we were interested in testing BIN1 and Dyn2, we first analyzed their phosphoinositide lipid-binding specificity. We used the proximity-based labeling of membrane-associated proteins (PLiMAP) assay, which monitors membrane binding based on proximity-based cross-linking of proteins to a bifunctional lipid probe containing a photoactivable diazirine moiety at the head and a fluorophore (BODIPY FL or BODIPY TMR) at the tail of phosphatidylethanolamine (35, 36). On liposomes containing 5 mol% of different phosphoinositide lipids and 1 mol% of the bifunctional probe in the background of DOPC, BIN1 displays a binding preference in the order of PI(4, 5)$P_2$ > PI(3, 4, 5)$P_3$ > PI(3, 4)$P_2$ = PI(3)P > PI(3, 5)$P_2$ ≫ PI(4P) > PI(5)P (*SI Appendix*, Fig. S1*C*). The apparent binding affinity of BIN1 for PI(4, 5)$P_2$ was ~0.13 μM (*SI Appendix*, Fig. S1*D*), which falls in the range of previous estimates (37). On the other hand, Dyn2 displays a binding preference in the order of PI(4, 5)$P_2$ > PI(3, 4)$P_2$ > PI(3, 4, 5)$P_3$ > PI(3, 5)$P_2$ ≫ PI(3)P ≫ PI(4P) = PI(5)P (*SI Appendix*, Fig. S1*C*). Since PI(4, 5)$P_2$ is the preferred phosphoinositide lipid for both BIN1 and Dyn2, we tested bilayer islands with 5 mol% of PI(4, 5)$P_2$ and 15 mol% DOPS in the background of DOPC. The lipid mixture contained 0.5 mol% of the fluorescent lipid analogue Texas Red-DHPE. Flowing 1 μM of the PI(4, 5)$P_2$ sensor mEGFP-PLCδ PH domain showed uniform binding to the island with no apparent effect on membrane morphology (*SI Appendix*, Fig. S1*E*). This confirms that PI(4, 5)$P_2$ is readily accessible and uniformly distributed on the island, and that the templates are stable to protein binding.

Remarkably, flowing 0.2 μM BIN1-mEGFP caused rapid and profuse tubulation of the island, which in turn caused the bilayer to retract and shrink in size (Fig. 1*A* and Movie S1). In contrast, flowing a 12-fold higher concentration of 2.5 μM BIN1 on SLBs formed by liposome fusion on glass showed protein binding but no apparent tubulation (*SI Appendix*, Fig. S1*F*), signifying that cushioned bilayer islands are readily amenable to membrane tubulation. After 10 min, BIN1-exposed bilayer islands displayed bright tubules that formed an extensive network (Fig. 1*B*, white arrows), which was also confirmed in scanning electron micrographs (SEM) (Fig. 1*C*, white arrows). This was because BIN1 tubules showed a tendency to coil around each other (Fig. 1*D* and Movie S2). Photobleaching the fluorescent lipid probe in a large region of the island displaying a BIN1-coated tubular network showed fluorescence recovery with time (*SI Appendix*, Fig. S1*G* and Movie S3). Fluorescence on BIN1-coated tubules recovers to the same extent as that seen on the underlying bilayer (*SI Appendix*, Fig. S1*H*), indicating that the tubules are connected to the island.

Next, we imaged the BIN1-induced tubulation reaction at a high frame rate and analyzed tubules before they began to coil. The mild flow of buffer laid down emergent tubules, which allowed them to be easily imaged (Fig. 1*E* and Movie S4). Tubules grew at an apparent rate of ~0.9 μm $s^{-1}$ (Fig. 1*F*). From a fluorescence-based calibration procedure, the estimated size of tubules was ~17 nm in radius (Fig. 1*G*), which agrees well with the scaffold dimension from cryo-electron microscopy (cryo-EM) reconstructions of BIN1-coated liposomes (38) and our previous estimates of BIN1 scaffolds on membrane nanotubes (39). Because of their tendency to coil rapidly, we were unable to verify tubule sizes from SEM.

To monitor early stages of the tubulation reaction, we flowed a low concentration of 50 nM BIN1 and imaged the island. The protein first bound uniformly and with time organized into foci, which likely represent oligomers, that diffused on the island (Fig. 1*H*, white arrow, Movie S5). Foci that were relatively less mobile and therefore easier to track in both the protein and membrane channels showed a coincident enrichment in BIN1 and membrane fluorescence, implying that the BIN1 oligomer tubulates the underlying bilayer (Fig. 1*I*). We analyzed the kinetics of this process on the less mobile BIN1 foci, which were identified by overlaying time-lapse images of BIN1 on the bilayer acquired 10 s apart (*SI Appendix*, Fig. S2*A*). Tracking fluorescence changes on one such oligomer in time showed a sharp rise in both BIN1 and membrane fluorescence, signifying kinetics of nucleation and growth of a BIN1 tubule (*SI Appendix*, Fig. S2*B*). Surprisingly, the onset of rise in BIN1 fluorescence occurred before the onset of rise in membrane fluorescence (*SI Appendix*, Fig. S2*C*). Indeed, a cumulative analysis of several independent events showed this to be a consistent feature, with the onset of rise in BIN1 and membrane fluorescence being separated by almost 20 s (Fig. 1*J*). This indicates that BIN1 first forms an oligomer that is likely flat in topology, which grows by recruiting molecules from solution and eventually acquires curvature and the capacity to tubulate the membrane. Thus, BIN1 oligomerization and membrane tubulation are sequential and not concurrent processes. It is however likely that such a trend reflects the behavior of the relatively less mobile BIN1 foci analyzed here.

**CNM-Linked BIN1 Mutants Are Defective in Membrane Binding and Tubulation.** The BIN1 N-BAR domain comprises a trihelical coiled-coil domain that forms a crescent shaped dimer with positively charged residues on the concave, membrane binding surface (Fig. 2*A*) (40). Despite their structural similarity, BIN1 shows significant differences compared to other BAR

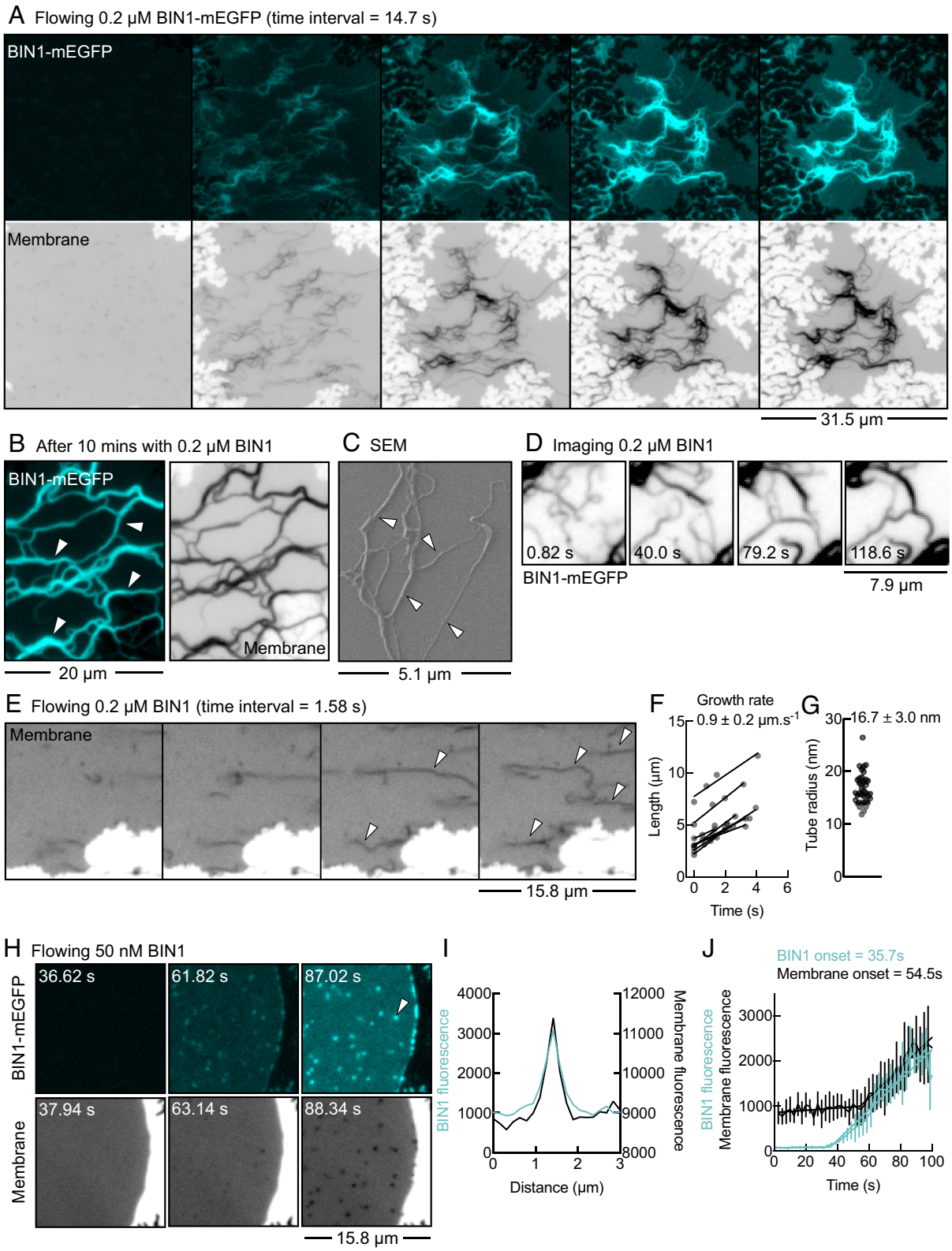


**Fig. 1.** Dynamics of BIN1-induced membrane tubulation. (*A*) Time-lapse images from Movie S1 of a bilayer island exposed to BIN1-mEGFP. The membrane is colored in gray and inverted in contrast. Fluorescence (*B*) and scanning electron microscopic (*C*) images showing BIN1 tubules on the bilayer island after 10 min. The membrane is colored in gray and inverted in contrast. Tubules are marked by white arrows. (*D*) Time-lapse images from Movie S2 showing coiling of BIN1 tubules. BIN1-mEGFP is colored in gray and inverted in contrast. (*E*) Time-lapse images from Movie S4 showing initiation and growth of BIN1 tubules, marked by white arrows. BIN1-mEGFP is colored in gray and inverted in contrast. (*F*) Plot showing growth rate of BIN1 tubules. Time is normalized to when tubules became apparent. Data represent the mean ± SD of nine tubules. (*G*) Plot showing the radius of BIN1 tubules. Data represent the mean ± SD radius of 37 separate and uncoiled tubules. (*H*) Time-lapse images from Movie S5 showing the formation of BIN1-mEGFP oligomers on the bilayer island. The membrane is colored in gray and inverted in contrast. (*I*) Fluorescence profile showing that the BIN1 oligomer, marked by the white arrow in (*H*), coincides with high membrane fluorescence. (*J*) Plot showing kinetics of BIN1 oligomerization and membrane tubulation fitted to a segmental linear regression equation. Data represent the mean ± SD of fluorescence intensities of five independent events.

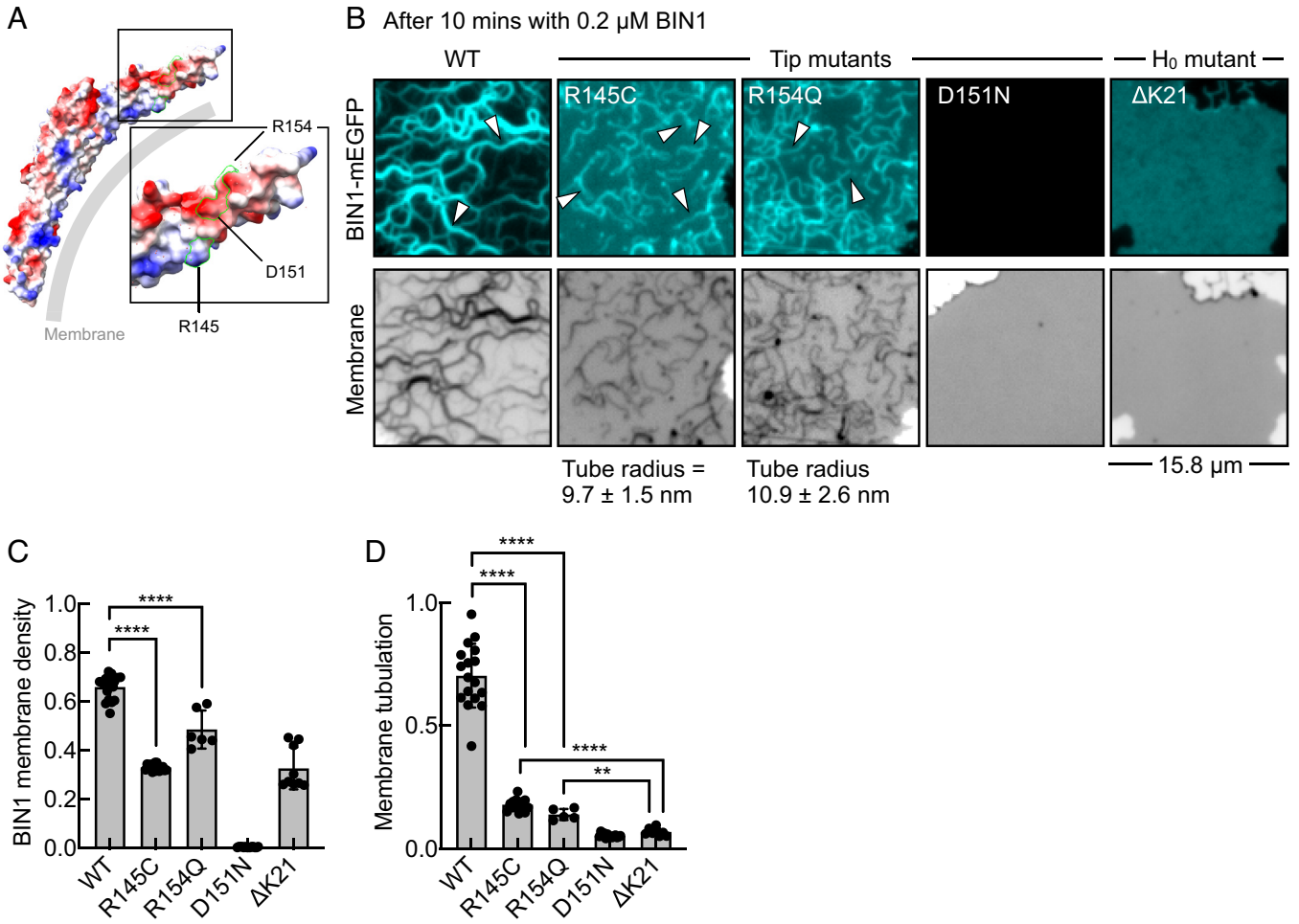


**Fig. 2.** CNM-linked BIN1 mutants are defective in membrane binding and tubulation. (*A*) Structure of the BIN1 N-BAR domain (PDB: 2FIC) rendered as a space filling model and colored based on electrostatics using ChimeraX (45). The structure marks the tip residues. (*B*) Fluorescence images showing the distribution of WT and the indicated mutants on a bilayer island. The membrane is colored in gray and inverted in contrast. White arrows in WT, R145C, and R154Q panels mark membrane tubules. Data represent the mean ± SD radius of 47 and 33 separate and uncoiled tubules for R145C and R154Q, respectively. (*C*) Plot showing membrane density of WT and CNM-linked BIN1 mutants measured as the BIN1-mEGFP to membrane fluorescence ratio. Data represent the mean ± SD of fluorescence ratio on 6 to 18 ROIs on multiple bilayer patches. Statistical significance was estimated using Mann–Whitney's test where **** denotes $P < 0.0001$. (*D*) Membrane tubulation defined as the increase of membrane fluorescence over bilayer fluorescence for WT and mutants. Data represent the mean ± SD of fluorescence on 6 to 18 ROIs on multiple bilayer patches. Statistical significance was estimated using Mann–Whitney's test where **** denotes $P < 0.0001$ and ** denotes $P = 0.0016$.

domain–containing proteins (38). BIN1 tubules are more rigid because of additional interactions between neighboring BAR domains and tighter protein packing on the tubule (38). Cryo-EM reconstructions indicate that one tip (residues 130 to 190) of the N-BAR dimer wedges into the membrane while the other points outward. Tip insertion into the membrane facilitates optimal packing of the oligomer (38). As is the case for other N-BAR proteins, the unstructured N-terminal region forms an amphipathic $H_0$ helix upon binding membranes and its insertion bends the membrane and stabilizes protein–protein contacts in the packed oligomer (40–42). Furthermore, tip residues have also been shown to become ordered upon membrane insertion (41). Importantly, mutations in the tip and the $H_0$ helix residues are linked to CNM and previous analyses have shown defects in membrane binding and tubulation (10, 21, 43). A more recently identified tip mutant R145C is also linked to CNM (44).

We tested the tip and $H_0$ helix mutants on bilayer islands. We flowed 0.2 μM of these mutants and waited for 10 min. Following this, we washed off excess protein and imaged the bilayer. These experiments showed that the tip mutants R145C and R154Q bound the membrane and were able to form tubules (Fig. 2*B*). Membrane binding was quantified by estimating the protein to membrane fluorescence ratio in a region of interest (ROI) on the bilayer. Such analysis revealed significant defects in membrane binding in the mutants compared to that seen with WT under similar conditions (Fig. 2*C*). Tubulation leads to an increase in fluorescence of the bilayer because of the higher membrane area in the optical path. We quantified the increase in membrane fluorescence in an ROI on the bilayer as a measure of the extent of tubulation. Such analysis revealed that R145C and R154Q tubulated membranes to a significantly lower extent than WT (Fig. 2*D*). Tubules formed with these mutants had a radius of ~10 nm for R145C and ~11 nm for R154Q (Fig. 2*B* and Movies S6 and S7), significantly thinner than that seen with WT (Fig. 1*G*) ($P < 0.001$, Mann–Whitney's test). Thus, these mutations reduce binding and tubulation but surprisingly organize into forming a scaffold of thinner dimensions. In contrast, the other tip mutant D151N showed no binding to the bilayer (Fig. 2 *B* and *C*), consistent with earlier results on PI(4, 5)$P_2$-containing membranes (43). Importantly, the $H_0$ helix mutant ΔK21 showed binding but no tubulation (Fig. 2 *B*–*D*), thus emphasizing the important role of $H_0$ helix insertion in membrane tubulation. The CNM-linked

mutations therefore appear to cause distinct and separable effects on BIN1 functions in membrane binding and tubulation. R145C and R154Q are partially defective in tubulation which likely arises from a defect in membrane binding, D151N abrogates membrane binding, while ΔK21 can bind but is defective in tubulation.

**BIN1 and Dyn2 Comprise a Minimal Two-Component MTCF Module.** Besides membrane tubulation, BIN1 recruits dynamin during the formation of T-tubules in muscle cells (20, 21, 25, 46). Flowing just Dyn2 onto cushioned bilayers showed no significant binding to the planar bilayer, but it bound preexisting buds and tubes (Fig. 3*A*, white arrows and Fig. 3*B*), consistent with its preference for binding membranes of high curvature (39, 47). Bilayer islands therefore present a significant advantage because it would report Dyn2 functions only in response to membrane tubulation. To recreate a physiological scenario where both proteins encounter each other, we flowed a premixed solution of BIN1, Dyn2, and GTP onto the bilayer islands. Remarkably, this produced an outcome quite different from the extensive tubulation seen with BIN1 alone (Fig. 1*A*). The islands now displayed numerous bright foci (Fig. 3*C* and Movie S8), which appeared as buds in SEM (Fig. 3*D*). Importantly, bleaching the fluorescent lipid probe showed recovery on the underlying bilayer but not in foci (Fig. 3*E* and Movie S9) and seen in the recovery plot (Fig. 3*F*). Since BIN1 (*SI Appendix*, Fig. S1 *G* and *H*) and dynamin (48) do not impose a lipid diffusion barrier, the lack of fluorescence recovery in the foci indicates that the foci/buds are severed vesicles. The severed vesicles contained both BIN1 and Dyn2 indicating that Dyn2 remains associated with BIN1 even after fission (Fig. 3*C*). We are unsure why the vesicles remain tethered to the island but multivalent interactions between BIN1 and Dyn2 on the vesicle and the bilayer could have contributed to the tethering. Together, these results indicate that BIN1 and Dyn2 comprise a minimal two-component module that can manage MTCF.

Replacing BIN1 with a construct lacking the SH3 domain (BIN1ΔSH3) showed tubulation but no fission (Fig. 3*G*), indicating that Dyn2 requires to be bound to BIN1 for fission. Furthermore, fission required a high relative concentration of Dyn2. Thus, reactions with equimolar concentrations of Dyn2 and BIN1 or even with a twofold molar excess of Dyn2 showed only tubulation and no fission (Fig. 3*H*). The binding affinity of the BIN1 SH3 domain for the Dyn2 PRD is ~70 μM (37) and recent analysis reports an affinity of the BIN1 SH3 domain for Dyn2 to be ~90 μM (11). But Dyn2 was present on BIN1 tubules under conditions that showed no fission (Fig. 3*H*) or throughout reactions that led to the formation of vesicles (Fig. 3*C*). Therefore, the requirement of high relative concentrations of Dyn2 for fission is quite unexpected and cannot be attributed solely to the low binding affinity between these proteins.

**Pathway to MTCF.** Dual-channel time-lapse imaging revealed the fleeting appearance of tubular intermediates that were positive for BIN1-mEGFP and Dyn2-mCherry (Fig. 4*A*, white arrows and Movie S8). To better analyze this reaction, we recorded time-lapse images of BIN1-mEGFP mixed with excess Dyn2 at a high frame rate, for which imaging was restricted to a single channel. In the absence of GTP, flowing this mixture formed tubules from the bilayer island (Fig. 4*B*, black arrows, Movie S10). Tubules grew at a rate of ~1 μm $s^{-1}$ (Fig. 4*C*), similar to that seen before with just BIN1 (Fig. 1*F*). Thus, the presence of Dyn2 does not affect the tubule growth rate. Furthermore, tubules grew while remaining tethered to the island (Fig. 4*B*, black arrows) and the fact that they grew at a rate like that seen in the absence of Dyn2 (Fig. 1*F*) suggests that the growth rate reflects an intrinsic property of BIN1 oligomerization and is not influenced by tethering or buffer flow. Eventually, tubules started coiling upon themselves or with other tubules in the vicinity and coalesced into bright foci (Fig. 4*B*, green arrows). Flowing a mixture of BIN1 and Dyn2 in the presence of GTP led to the formation of tubules (Fig. 4*D*, black arrows), which quickly got severed (Fig. 4*D*, yellow arrows, Movie S11). Tubules sometimes displayed more than one fission event resulting in the formation of multiple tubule fragments. As was seen in the absence of GTP, tubules showed a tendency to coil before or after fission and coalesce into bright foci (Fig. 4*D*, green arrows). Tubules grew at a rate of ~0.8 μm $s^{-1}$ (Fig. 4*E*) and the time interval between the appearance and fission of a tubule for a number of such events was ~5 s (Fig. 4*F*), which puts the fission rate at ~0.2 $s^{-1}$.

**Mechanistic Basis for MTCF.** Our results suggest that membrane tubulation and fission are temporally linked, i.e., tubules grow for a while before fission is apparent (Movie S11). This could merely arise from Dyn2's preference for binding high curvature tubules such that fission manifests only upon the formation of a BIN1 tubule. But results with BIN1ΔSH3 indicate that the formation of a tubule of high curvature is by itself not sufficient for fission. This suggests that Dyn2 incorporated in the growing BIN1 tubule must be inhibited in fission and the requirement for high relative concentrations of Dyn2 could reflect the necessity to overcome this inhibition.

The obligatory requirement of BIN1 for tubulation makes it difficult to analyze the effects of BIN1 on Dyn2 functions. We therefore turned to analyzing Dyn2 functions on preformed nanotubes of the same lipid composition as bilayer islands. Control experiments revealed that BIN1 facilitates the recruitment of Dyn2 onto nanotubes of a wide range of sizes via the SH3 PRD interaction (*SI Appendix*, Fig. S3 *A* and *B*). Flowing 0.1 μM Dyn2 with GTP caused rapid and processive severing of nanotubes (Movie S12). We then analyzed the effect of flowing 0.1 μM Dyn2 and GTP mixed with increasing concentrations of BIN1. Imaging the nanotubes after 10 min revealed fission till a concentration of 0.6 μM BIN1 (Fig. 5*A*). At 0.6 μM BIN1, nanotubes were completely refractory to fission (Movie S13). This is apparent from estimates of the fraction of nanotubes showing at least one cut after 10 min (Fig. 5*B*, black dataset). Time-lapse imaging revealed inhibitory effects even at lower BIN1 concentrations. This is apparent from estimates of the frequency of cuts on individual nanotubes after a short 2 min interval (*SI Appendix*, Fig. S3*C*, black data). BIN1 therefore inhibits Dyn2-catalyzed membrane fission in a dose-dependent manner.

The N-BAR and SH3 domain–containing protein endophilin inhibits Dyn1 functions by interfering with the formation of Dyn1 scaffolds, which is necessary for stimulated GTP hydrolysis and fission (49). But a mechanism involving structural inhibition should have influenced BIN1 tubule growth rates in the presence of Dyn2, especially when they are both present on the tubule, which is not the case (Figs. 1*F* and 4*C*). How then can the inhibition of Dyn2 functions by BIN1 be explained? To address this, we performed a coupled liposome cosedimentation and PLiMAP assay with Dyn2 and BIN1. Cosedimentation reports on the total levels of liposome-associated proteins while PLiMAP reports on their proximity to the membrane interface, which is a more stringent measure of membrane binding. Liposomes were incubated with 0.3 μM Dyn2 mixed with a range of BIN1 concentrations and incubated for 30 min. The mixture was then exposed to UV and sedimented. In the absence of BIN1, a substantial fraction of Dyn2 cosediments with liposomes (Fig. 5*C*, CBB panel), and is also fluorescent

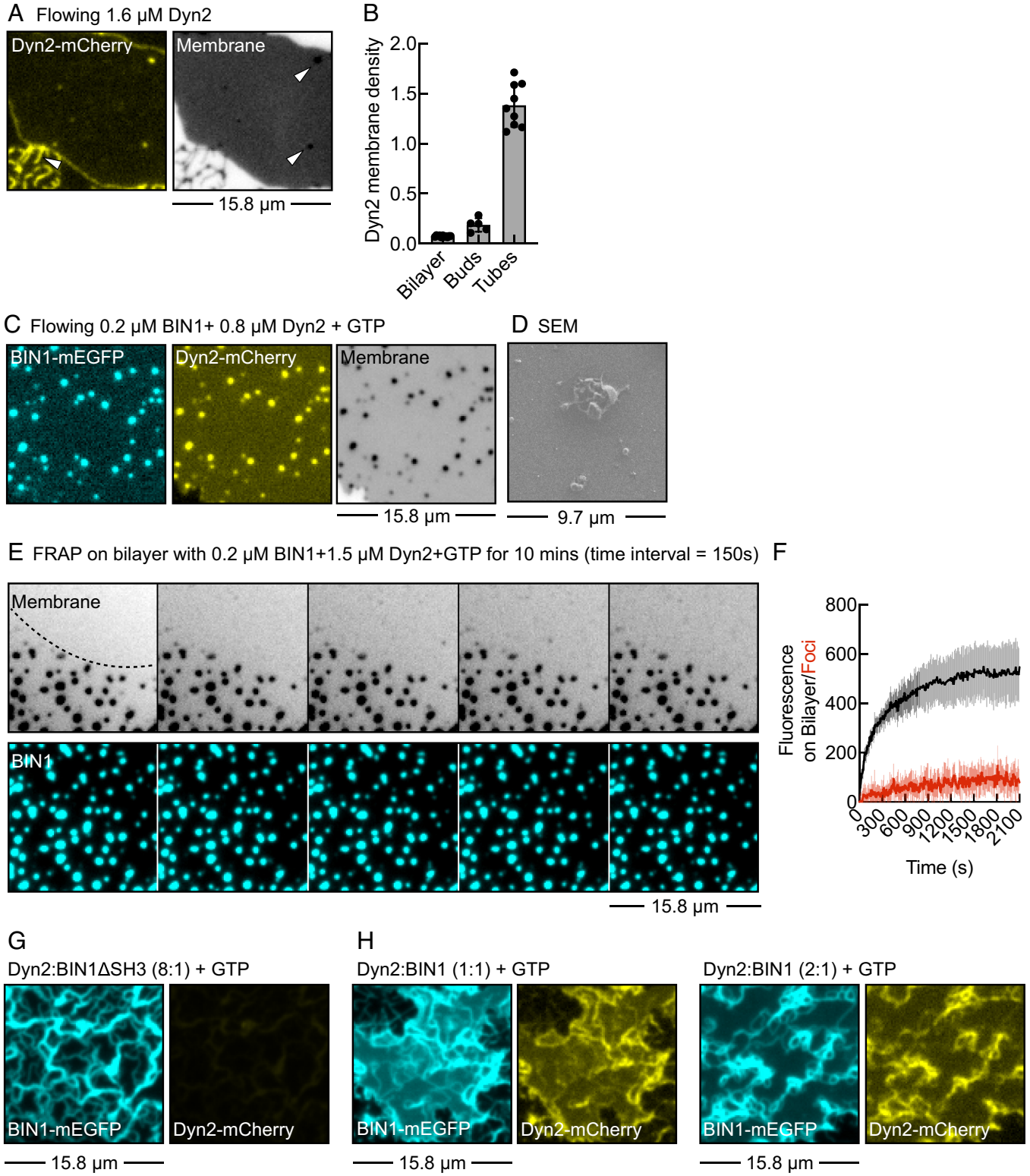


**Fig. 3.** BIN1 and Dyn2 comprise a minimal two-component module that can manage MTCF. (*A*) Fluorescence image showing the distribution of Dyn2-mCherry on the bilayer island. Dyn2-mCherry is colored in yellow, and the membrane is colored in gray and inverted in contrast. White arrows mark preexisting buds on the island. (*B*) Plot showing membrane density of Dyn2 measured as the ratio of Dyn2-mCherry and membrane fluorescence on bilayers, buds, and tubules. Data represent the mean ± SD of 11 bilayer patches, 5 buds, and 9 tubules. Fluorescence (*C*) and scanning electron microscopic (*D*) images of a bilayer island exposed to BIN1 with excess Dyn2 and GTP. The membrane is colored in gray and inverted in contrast. (*E*) Time-lapse images from Movie S9 showing recovery after bleaching the fluorescent lipid probe in a large area of the bilayer island exposed to BIN1 with Dyn2 and GTP. The dotted line represents the boundary of the bleached region. The membrane is colored in gray and inverted in contrast. (*F*) Plots showing fluorescence recovery of the lipid probe on the bilayer (black) and on foci (red). Data represent the mean ± SD of fluorescence on 10 foci and the underlying bilayer. (*G*) Fluorescence image showing the distribution of BIN1ΔSH3-mEGFP and Dyn2-mCherry. Bilayers were imaged after 10 min incubation with 0.2 μM BIN1ΔSH3-mEGFP and 1.5 μM Dyn2-mCherry with 1 mM GTP followed by a wash-off with buffer. (*H*) Fluorescence image showing the distribution of BIN1-mEGFP and Dyn2-mCherry in presence of GTP. Bilayers were imaged after 10 min of incubation with 0.2 μM BIN1-mEGFP and 0.2 μM or 0.4 μM Dyn2-mCherry with 1 mM GTP followed by a wash-off with buffer.

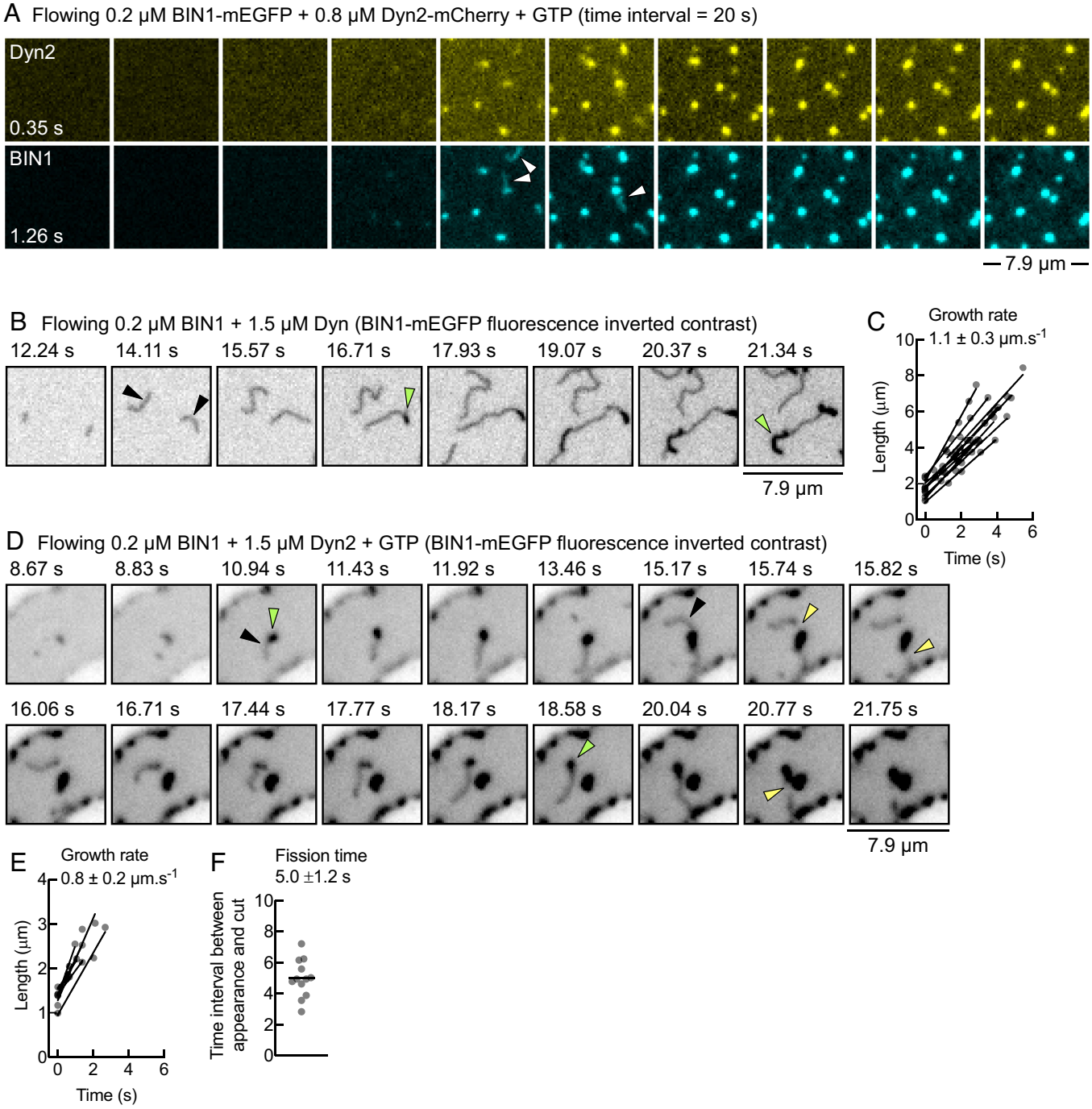


**Fig. 4.** Pathway to MTCF. (*A*) Time-lapse images from Movie S8 of bilayer islands exposed to the indicated concentrations of BIN1-mEGFP and Dyn2-mCherry with 1 mM GTP. White arrows mark tubular intermediates. (*B*) Time-lapse images of a bilayer island exposed to the indicated proteins in the absence of GTP. Black arrows mark single tubules and green arrows mark coiled regions. See Movie S10. (*C*) Plot showing the growth rate of BIN1 tubules under conditions described in (*B*). Data represent the mean ± SD of 10 tubules. (*D*) Time-lapse images of a bilayer island exposed to the indicated proteins in the presence of GTP. Black arrows mark single tubules, green arrows mark coiled regions and yellow arrows mark fission. See Movie S11. (*E*) Plot showing the growth rate of BIN1 tubules under conditions described in (*D*). Data represent the mean ± SD of six tubules. (*F*) Plot showing the fission time, defined as the time interval between appearance and fission of a tubule. Data represent the mean ± SD of 12 events.

(Fig. 5*C*, fluor panel), indicating that readouts from cosedimentation and PLiMAP are consistent with each other. Increasing BIN1 concentrations causes a small but significant increase in Dyn2 levels on the membrane. This is apparent from a quantitative densitometric analysis of Dyn2 levels in the pellet (Fig. 5*C*, CBB panel and Fig. 5*D*). This is consistent with BIN1 facilitating recruitment of Dyn2 on nanotubes (*SI Appendix*, Fig. S3 *A* and *B*). But surprisingly, the fluorescence signal of Dyn2 in the pellet shows a significant decline, with an 80% reduction at a 1:6 Dyn2:BIN1 ratio (Fig. 5 *C* and *D*). Thus, increasing BIN1 levels recruits more Dyn2 but lowers the fraction of membrane-bound Dyn2. This could explain the inhibition in fission seen with higher BIN1 concentrations (Fig. 5 *A* and *B*). Since the inhibition is dose-dependent, increasing Dyn2 concentration would overcome this inhibition and explains why fission requires a high relative concentration of Dyn2. Tubules formed with BIN1ΔSH3 are resilient to fission, signifying that the SH3-PRD interaction helps overcome the inhibition likely because the multivalent SH3-PRD interaction would help attain the critical Dyn2 concentration required for fission on the tubule at a lower bulk Dyn2 concentration.

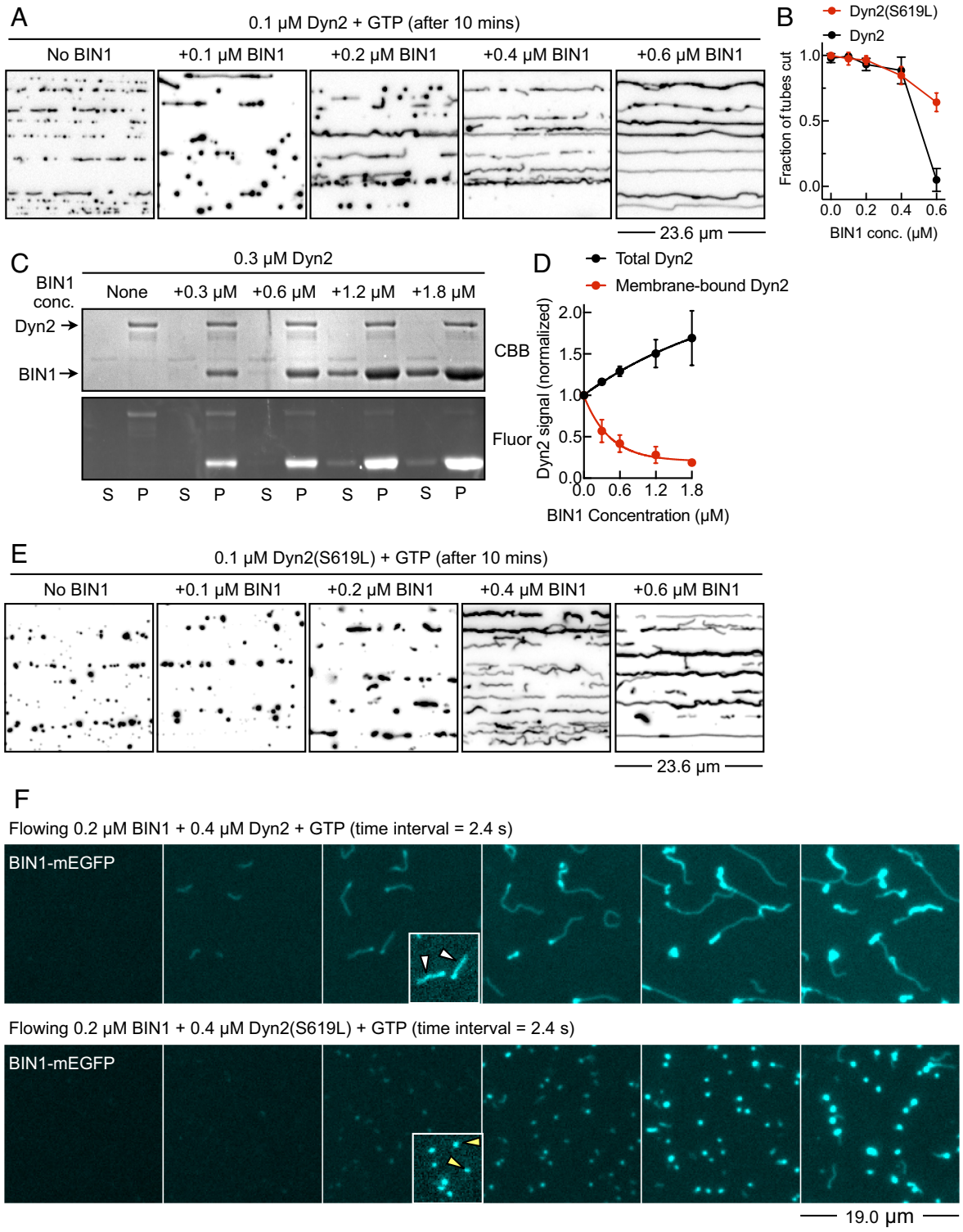


**Fig. 5.** Mechanistic basis for MTCF. (*A*) Fluorescence images of membrane nanotubes after being exposed to 0.1 μM Dyn2 with GTP for 10 min. The membrane is colored in gray and inverted in contrast. (*B*) Plot showing the fraction of nanotubes showing at least one cut in presence of 0.1 μM Dyn2 (black) or 0.1 μM Dyn2(S619L) (red) and 1 mM GTP with increasing concentrations of BIN1. Data represent the mean ± SD from six separate fields of nanotubes. (*C*) Results from a coupled liposome cosedimentation and PLiMAP experiment showing in-gel fluorescence (Fluor) and Coomassie brilliant blue (CBB) staining of Dyn2 and BIN1 in the supernatant (S) and pellet (P) fractions. (*D*) Plot showing densitometric (black) and fluorescence (red) quantitation of Dyn2 in the pellet fraction. Data represent the mean ± SD from two independent experiments. (*E*) Fluorescence images of membrane nanotubes after being exposed to 0.1 μM Dyn2(S619L) with GTP for 10 min. The membrane is colored in gray and inverted in contrast. (*F*) Time-lapse images from Movie S14 showing the bilayer island exposed to the indicated concentrations of proteins with 1 mM GTP. *Insets* show magnified images of intermediates adjusted in contrast for clarity. White arrows mark tubules and yellow arrows mark vesicles.

Dyn2 binds PI(4, 5)$P_2$ in the membrane through the pleckstrin-homology domain (PHD). Our results indicate that BIN1 inhibits Dyn2 functions by reducing its membrane binding. The PHD binds the stalk domain of Dyn2 in solution (50). The stalk domain mutation S619L interferes with this binding and relieves autoinhibition thereby facilitating Dyn2 oligomerization. But this mutation also enhances Dyn2's membrane binding and facilitates fission (25, 46, 51). Importantly, the S619L represents a CNM-linked gain-of-function mutation (18, 52, 53). On membrane nanotubes, increasing concentrations of BIN1 only partially inhibited the Dyn2(S619L)-catalyzed fission (Fig. 5*E*). Thus, in the presence of 0.6 μM BIN1, while Dyn2 showed no fission (Fig. 5*A*), the fraction of severed tubes with Dyn2(S619L) rose to ~0.75 (Fig. 5*B*, red data). This effect is more apparent on the frequency of cuts on individual nanotubes after 2 min of the fission reaction where Dyn2(S619L) showed a significantly higher fission efficiency than Dyn2 (*SI Appendix*, Fig. S3*C*) and was less susceptible to BIN1-mediated inhibition than Dyn2 (Fig. 5*B*, red data). Finally, we tested Dyn2(S619L) mixed with BIN1 on bilayer islands. As shown earlier, reactions with twofold molar excess of Dyn2 over BIN1 showed only tubulation and no fission (Fig. 3*H*). This is apparent in time-lapse images of the bilayer island exposed to 0.2 μM BIN1 and 0.4 μM Dyn2 with GTP (Fig. 5*F* and Movie S14), where tubules grew and because coiled. But reactions with 0.2 μM BIN1 and 0.4 μM Dyn2(S619L) with GTP showed remnants of severed tubules, which appeared as foci, indicative of fission (Fig. 5*F* and Movie S14). The difference is more apparent at early time points where mixtures containing WT Dyn2 showed longer tubules while those with Dyn2(S619L) showed numerous foci (Fig. 5 *F*, *Inset*).

## Discussion

Here, we establish a facile planar bilayer template and a broadly applicable workflow for analyzing dynamics of membrane tubulation and its subsequent fission. Using these templates, we present insights into early steps in the tubulation reaction and mechanisms that regulate MTCF. Thus, MTCF is an emergent phenomenon that arises from a molecular coordination between a BAR domain protein and dynamin wherein the BAR domain protein recruits but inhibits dynamin functions. Furthermore, we evaluate functions of CNM-associated mutants in BIN1 and Dyn2 and our results establish a causal link between MTCF and the CNM pathology. Together, our results highlight the potential of cushioned planar bilayer islands for analyzing cellular processes involving membrane tubulation and fission through reconstitution.

Previous analysis from negative-stain EM of the BIN1 N-BAR domain shows that deletion of the tip portion (residues 147 to 176) or the R154Q mutant forms tubules of a similar size as WT but the internal order in arrangement of protein subunits is lost (38, 43). So, loss of tip residue interactions renders BIN1 to form a loose protein scaffold on the tubule. The difference between our estimates and those reported earlier could arise from the analysis of tubules drawn out of a planar bilayer island, where the membrane tension is low, compared to those on liposomes. The size of a BIN1-coated tubule likely reflects a balance between protein scaffolding mediated by tip-residue interactions and membrane wedging mediated by insertion of the $H_0$ helix. Our results indicate that weakening of tip-residue interactions causes the tubules to become thinner, which likely manifests from the wedging effect becoming dominant. Future structural analyses of tubules drawn from planar bilayer islands would address this aspect.

The influence of BAR domain proteins on dynamin-catalyzed membrane fission has been extensively studied, but results differ depending on the choice of the assay system and the specific set of proteins tested (26). GUV-based experiments have indicated that amphiphysin1 and endophilin 1 facilitate dynamin recruitment to the membrane, thereby causing their shrinkage which was assumed to reflect vesiculation (54). On the other hand, results using SUPER templates, where vesiculation can be quantitated by a bulk measurement of released vesicles have shown that amphiphysin1 facilitates dynamin-dependent vesiculation while endophilin1 does not (23). More recently, a mixture of BIN1 and Dyn2 was shown not to vesiculate SUPER templates (25). Our results indicate that fission is sensitive to the relative levels of the BAR domain protein and Dyn2. Thus, a likely cause for the discrepancy is because some of the previous studies have not tested a dose-dependent effect of Dyn2 on fission. Furthermore, we find that severed BIN1-coated tubules remain tethered to the bilayer, which would complicate readouts from a SUPER template pelleting assay that relies on quantitating released vesicles. Our results with cushioned bilayers show that Dyn2 does not bind these planar membranes and that tubulation by BIN1 serves to recruit Dyn2. This is likely also the case for proteins like amphiphysin1 and endophilin1, which could facilitate dynamin recruitment to the membrane by their combined ability to bind dynamin and tubulate the membrane. The ability to directly visualize and correlate protein recruitment and membrane tubulation with fission, which has not been possible with GUVs or SUPER templates, emphasizes the potential of cushioned bilayer templates. But on membrane nanotubes which by themselves support dynamin binding and fission, BAR domain proteins inhibit dynamin functions (26). This is consistent with what we observe with BIN1. Previous studies have established that BAR domain proteins serve as adaptors to recruit dynamin to the membrane (25, 26, 54). In most cases, Dyn2 recruitment was assayed using liposome pelleting or fluorescence microscopy and our results with BIN1 are consistent with these reports. In addition to a protein-based interaction, BIN1's ability to induce clustering of PI(4, 5)$P_2$ via its N-BAR domain has been suggested as a mechanism for dynamin recruitment (24). Such a mechanism could contribute to the cooperative recruitment of dynamin as well as BIN1 to the membrane. But our results from testing BIN1 and Dyn2 interaction at varying stoichiometries inform of a mechanism whereby an adaptor recruits but inhibits dynamin's membrane binding. This has been revealed because of a proximity-based lipid cross-linking assay coupled with liposome cosedimentation. A likely mechanism by which BIN1 inhibits Dyn2's membrane binding is by the PI stretch in BIN1 sequestering PI(4, 5)$P_2$ and making it unavailable for dynamin. This is consistent with observations that the inhibitory effect of BIN1 on Dyn2 can be overcome by the S619L mutation, which confers Dyn2 with a higher membrane binding affinity. Such a mechanism might have uniquely evolved in BIN1 because of its function in forming stable T-tubules. On the other hand, BAR domain proteins that are involved in fast endocytic trafficking such as amphiphysin1 and endophilin1 might not impose such inhibition on dynamin function because they lack the PI stretch.

Our results provide insights into the functional partnership between BIN1 and Dyn2. CNM-linked BIN1 and Dyn2 mutants tested here display aberrant functions in membrane tubulation and fission and these results become relevant in understanding CNM-like pathology. The architecture of stable T-tubules in tissues has been well studied but an understanding of the early steps in their biogenesis is only beginning to emerge. Live imaging of T-tubule development in zebrafish embryos suggests a pathway wherein BIN1 along with other proteins form dynamic endocytic tubules at the plasma membrane, some of which are captured and

stabilized by contacts with the sarcoplasmic reticulum (5). This endocytic capture model highlights similarities between early stages of T-tubule biogenesis and clathrin-independent trafficking pathways that involve a tubular membrane intermediate. Recent work visualizing the plasma membrane of unroofed differentiated myotubes shows BIN1-positive tubules emanating from ring-like platforms composed of caveolar proteins (55). Dyn2 is a stable component of developing and mature T-tubules but surprisingly also functions to sever BIN1 tubules and a dysregulation of this process is linked to CNM (17, 18, 20, 21, 25, 46). Our results demonstrate that the relative levels of Dyn2 and BIN1 determine whether tubules remain intact or get severed. BIN1 competitively inhibits Dyn2 functions at the level of its membrane binding. At low ratios of Dyn2 and BIN1, this inhibition prevents severing of BIN1 tubules. High Dyn2 concentrations overcome this inhibition and render the BIN1 tubule susceptible to fission. BIN1 and Dyn2 levels are mutually regulated during muscle development (16). Perhaps, at early stages during development where Dyn2 levels are relatively high, fission of emergent BIN tubules acts as a quality control mechanism. Tubules that form contacts with the sarcoplasmic reticulum are left intact while others are pruned and turned over. Hypoactive BIN1 mutants would produce fewer and structurally defective tubules while hyperactive Dyn2 mutants would result in excessive pruning, both of which would lower tubule densities and eventually impact T-tubule architecture.

Our results provide insights into mechanisms that regulated MTCF, which could be relevant in vesicular transport. MTCF dynamics seen with BIN1 and Dyn2, where the tubule extends for a considerable length before undergoing fission, is reminiscent of several intracellular transport reactions involving a tubular intermediate (2, 3, 7). Pathways that form vesicular transport carriers, such as during clathrin-mediated endocytosis where the coat imposes a bud-like architecture on emergent transport intermediates are quite well-characterized in terms of mechanisms that regulate their budding and fission. The budding process defines a neck, which is the region with the highest membrane curvature, and drives the assembly of BAR proteins that eventually recruit dynamin for fission (13). On the other hand, mechanisms that coordinate growth and fission of tubular transport carriers (TTCs) remain less understood (56). TTCs are apparent in numerous clathrin-independent endocytic and endocytic recycling pathways (2, 3, 7, 57–59). For a TTC-based transport pathway to function optimally, membrane tubulation must be coordinated with fission. Excessive tubulation or premature fission would affect throughput of the transport reaction. Furthermore, tubules display the same membrane curvature along their entire length, so a mechanism that utilizes a gradient of curvature to define the fission site is untenable. Proteins such as sorting nexins (SNXs), which contain a membrane binding and bending domain are overrepresented in intracellular TTC-based transport pathways. SNXs contain a PX domain that binds phosphoinositide lipids and a BAR domain that forms a tubular scaffold or coat (59, 60). The presence of these domains would render SNXs capable of both initiating and progressively tubulating donor membranes. But our results suggest that the same features could also intrinsically regulate fission. Our results with BIN1, which also contains a membrane binding PI stretch and membrane bending BAR domain, inform of a mechanism that regulates MTCF. BIN1 recruits Dyn2 through SH3-PRD interactions but inhibits its membrane binding, likely because the PI stretch of BIN1 competes with the PHD of Dyn2 for $PI(4,5)P_2$ binding. This dual effect of potentiating recruitment but inhibiting membrane binding signifies a mechanism for how a protein scaffold regulates MTCF. While the exact mechanism that manages release of TTCs remains unclear, a similar competition for phosphoinositide lipids between the SNX coat and the putative fission catalyst could determine fission rates, thereby regulating the throughput of TTC-based transport pathways. Reconstituting such reactions using the membrane template described here represents an exciting avenue for future research.

## Methods

**Expression, Purification, and Fluorescent Labeling of Proteins.** Human BIN1-EGFP (isoform 8) (Addgene plasmid #27305) and human Dyn2-mCherry were cloned in pET15b with an N-terminal 6xHis and a C-terminal StrepII tag. Human dynamin 2 was cloned in pET15B with a C- terminal StrepII tag. Mutations were introduced using PCR. All clones were confirmed by sequencing. Proteins were purified as described in *SI Appendix*. For FRAP experiments, BIN1 was labeled with fivefold excess of Texas Red-C5-maleimide (Invitrogen) in 20 mM HEPES pH 7.4 with 150 mM NaCl. The reaction was quenched with excess DTT, and the unreacted dye was removed by extensive dialysis.

**PLiMAP.** PLiMAP assays with diazirine derivatives of BODIPY FL or BODIPY TMR phosphatidylethanolamine were carried out as described earlier (35, 36) and are detailed in *SI Appendix*.

**Field Emission Scanning Electron Microscopy.** Samples were fixed and processed for EM inside the flow chamber as described in *SI Appendix*.

**PEG-Cushioned Bilayer Islands and Membrane Nanotubes.** Membrane templates were formed on glass coverslips covalently conjugated with PEG400 or PEG8000 as described earlier (34) and detailed in *SI Appendix*.

**Fluorescence Imaging and Image Analysis.** Reactions were imaged through a 100x, 1.4 NA oil-immersion objective on an Olympus IX83 inverted microscope connected to an LED light source (CoolLED) and an Evolve 512 EMCCD camera (Photometrics). Image acquisition was controlled by μManager and images were analyzed using Fiji (61). Tubule sizes were estimated based on a calibration procedure as described earlier (34). Fluorescence image analysis routines are described in *SI Appendix*.

**Data, Materials, and Software Availability.** All study data are included in the article and/or supporting information.

**ACKNOWLEDGMENTS.** S.B. thanks the Indian Institute of Science Education and Research, Pune for a graduate fellowship. T.J.P. thanks the Howard Hughes Medical Institute for funding support. We thank Girish Deshpande and Pucadyil Lab members for comments on the manuscript.

1. S. W. Suzuki *et al.*, A PX-BAR protein Mvp1/SNX8 and a dynamin-like GTPase Vps1 drive endosomal recycling. *Elife* **10**, e69883 (2021).
2. E. Boucrot *et al.*, Endophilin marks and controls a clathrin-independent endocytic pathway. *Nature* **517**, 460–465 (2015).
3. H.-F. Renard *et al.*, Endophilin-A2 functions in membrane scission in clathrin-independent endocytosis. *Nature* **517**, 493–496 (2015).
4. L. Chan Wah Hak *et al.*, FBP17 and CIP4 recruit SHIP2 and lamellipodin to prime the plasma membrane for fast endophilin-mediated endocytosis. *Nat. Cell Biol.* **20**, 1023–1031 (2018).
5. T. E. Hall *et al.*, In vivo cell biological screening identifies an endocytic capture mechanism for T-tubule formation. *Nat. Commun.* **11**, 3711 (2020).
6. Z. Feng, C. Yu, $PI(3,4)P_2$-mediated membrane tubulation promotes integrin trafficking and invasive cell migration. *Proc. Natl. Acad. Sci. U.S.A.* **118**, e2017645118 (2021).
7. J. Carlton *et al.*, Sorting nexin–1 mediates tubular endosome-to-TGN transport through coincidence sensing of high- curvature membranes and 3-phosphoinositides. *Curr. Biol.* **14**, 1791–1800 (2004).
8. M. Ibrahim, J. Gorelik, M. H. Yacoub, C. M. Terracciano, The structure and function of cardiac t-tubules in health and disease. *Proc. R. Soc. B Biol. Sci.* **278**, 2714–2723 (2011).
9. L. Al-Qusairi, J. Laporte, T-tubule biogenesis and triad formation in skeletal muscle and implication in human diseases. *Skelet. Muscle* **1**, 26 (2011).
10. A. Hohendahl, A. Roux, V. Galli, Structural insights into the centronuclear myopathy-associated functions of BIN1 and dynamin 2. *J. Struct. Biol.* **196**, 37–47 (2016).
11. B. Zambo *et al.*, Uncovering the BIN1-SH3 interactome underpinning centronuclear myopathy. *eLife* **13**, RP95397 (2024).
12. E. Lee *et al.*, Amphiphysin 2 (Bin1) and T-tubule biogenesis in muscle. *Science* **297**, 1193–1196 (2002).

13. S. M. Ferguson, P. De Camilli, Dynamin, a membrane-remodelling GTPase. *Nat. Rev. Mol. Cell Biol.* **13**, 75–88 (2012).
14. H. Khurana, T. J. Pucadyil, "Gearing" up for dynamin-catalyzed membrane fission. *Curr. Opin. Cell Biol.* **83**, 102204 (2023).
15. C. Gineste, J. Laporte, Therapeutic approaches in different congenital myopathies. *Curr. Opin. Pharmacol.* **68**, 102328 (2023).
16. H. Perdreau-Dahl *et al.*, BIN1, myotubularin, and dynamin-2 coordinate T-tubule growth in cardiomyocytes. *Circ. Res.* **132**, e188–e205 (2023).
17. V. M. Lionello *et al.*, BIN1 modulation in vivo rescues dynamin-related myopathy. *Proc. Natl. Acad. Sci. U.S.A.* **119**, e2109576119 (2022).
18. R. Gómez-Oca *et al.*, Differential impact of ubiquitous and muscle dynamin 2 isoforms in muscle physiology and centronuclear myopathy. *Nat. Commun.* **13**, 6849 (2022).
19. R. Silva-Rojas *et al.*, Mice with muscle-specific deletion of Bin1 recapitulate centronuclear myopathy and acute downregulation of dynamin 2 improves their phenotypes. *Mol. Ther.* **30**, 868–880 (2022).
20. B. S. Cowling *et al.*, Amphiphysin (BIN1) negatively regulates dynamin 2 for normal muscle maturation. *J. Clin. Invest.* **127**, 4477–4487 (2017).
21. K. Fujise *et al.*, Mutant BIN1-dynamin 2 complexes dysregulate membrane remodeling in the pathogenesis of centronuclear myopathy. *J. Biol. Chem.* **296**, 100077 (2021).
22. S. Buono *et al.*, Reducing dynamin 2 (DNM2) rescues *DNM2* -related dominant centronuclear myopathy. *Proc. Natl. Acad. Sci. U.S.A.* **115**, 11066–11071 (2018).
23. S. Neumann, S. L. Schmid, Dual role of BAR domain-containing proteins in regulating vesicle release catalyzed by the GTPase, dynamin-2. *J. Biol. Chem.* **288**, 25119–25128 (2013).
24. L. Picas *et al.*, BIN1/M-Amphiphysin2 induces clustering of phosphoinositides to recruit its downstream partner dynamin. *Nat. Commun.* **5**, 5647 (2014).
25. J. Laiman *et al.*, GSK3α phosphorylates dynamin-2 to promote GLUT4 endocytosis in muscle cells. *J. Cell Biol.* **222**, e202102119 (2023).
26. O. Daumke, A. Roux, V. Haucke, BAR domain scaffolds in dynamin-mediated membrane fission. *Cell* **156**, 882–892 (2014).
27. T. J. Pucadyil, S. L. Schmid, Real-time visualization of dynamin-catalyzed membrane fission and vesicle release. *Cell* **135**, 1263–1275 (2008).
28. T. Itoh *et al.*, Dynamin and the actin cytoskeleton cooperatively regulate plasma membrane invagination by BAR and F-BAR proteins. *Dev. Cell* **9**, 791–804 (2005).
29. S. Mashaghi, A. M. Van Oijen, A versatile approach to the generation of fluid supported lipid bilayers and its applications: Engineering protein-functionalized membranes. *Biotechnol. Bioeng.* **111**, 2076–2081 (2014).
30. E. Karatekin, J. E. Rothman, Fusion of single proteoliposomes with planar, cushioned bilayers in microfluidic flow cells. *Nat. Protoc.* **7**, 903–920 (2012).
31. A.-L. Le Roux *et al.*, Dynamic mechanochemical feedback between curved membranes and BAR protein self-organization. *Nat. Commun.* **12**, 6550 (2021).
32. M. L. Wagner, L. K. Tamm, Tethered polymer-supported planar lipid bilayers for reconstitution of integral membrane proteins: Silane-polyethyleneglycol-lipid as a cushion and covalent linker. *Biophys. J.* **79**, 1400–1414 (2000).
33. T. J. Pucadyil, S. S. Holkar, Comparative analysis of adaptor-mediated clathrin assembly reveals general principles for adaptor clustering. *Mol. Biol. Cell* **27**, 3156–3163 (2016).
34. S. Dar, S. C. Kamerkar, T. J. Pucadyil, Use of the supported membrane tube assay system for real-time analysis of membrane fission reactions. *Nat. Protoc.* **12**, 390–400 (2017).
35. G. P. Jose, S. Gopan, S. Bhattacharyya, T. J. Pucadyil, A facile, sensitive and quantitative membrane-binding assay for proteins. *Traffic* **21**, 297–305 (2020).
36. G. P. Jose, T. J. Pucadyil, PLiMAP: Proximity-based labeling of membrane-associated proteins. *Curr. Protoc. Protein Sci.* **101**, e110 (2020).
37. T. Wu, T. Baumgart, BIN1 membrane curvature sensing and generation show autoinhibition regulated by downstream ligands and PI(4,5)$P_2$. *Biochemistry* **53**, 7297–7309 (2014).
38. J. Adam, N. Basnet, N. Mizuno, Structural insights into the cooperative remodeling of membranes by amphiphysin/BIN1. *Sci. Rep.* **5**, 15452 (2015).
39. H. Khurana, K. Baratam, S. Bhattacharyya, A. Srivastava, T. J. Pucadyil, Mechanistic analysis of a novel membrane-interacting variable loop in the pleckstrin-homology domain critical for dynamin function. *Proc. Natl. Acad. Sci. U.S.A.* **120**, e2215250120 (2023).
40. E. Casal *et al.*, The crystal structure of the BAR domain from human Bin1/Amphiphysin II and its implications for molecular recognition. *Biochemistry* **45**, 12917–12928 (2006).
41. J. M. Isas, M. R. Ambroso, P. B. Hegde, J. Langen, R. Langen, Tubulation by amphiphysin requires concentration-dependent switching from wedging to scaffolding. *Structure* **23**, 873–881 (2015).
42. C. Löw *et al.*, Structure and dynamics of helix-0 of the N-BAR domain in lipid micelles and bilayers. *Biophys. J.* **95**, 4315–4323 (2008).
43. T. Wu, Z. Shi, T. Baumgart, Mutations in BIN1 associated with centronuclear myopathy disrupt membrane remodeling by affecting protein density and oligomerization. *PLoS One* **9**, e93060 (2014).
44. M. Cabrera-Serrano *et al.*, A Roma founder *BIN1* mutation causes a novel phenotype of centronuclear myopathy with rigid spine. *Neurology* **91**, e339–e348 (2018).
45. E. F. Pettersen *et al.*, UCSF ChimeraX: Structure visualization for researchers, educators, and developers. *Protein Sci.* **30**, 70–82 (2021).
46. Y.-H. Chin *et al.*, Dynamin-2 mutations associated with centronuclear myopathy are hypermorphic and lead to T-tubule fragmentation. *Hum. Mol. Genet.* **24**, 5542–5554 (2015).
47. Y.-W. Liu *et al.*, Differential curvature sensing and generating activities of dynamin isoforms provide opportunities for tissue-specific regulation. *Proc. Natl. Acad. Sci. U.S.A.* **108**, E234–E242 (2011).
48. R. Deo *et al.*, ATP-dependent membrane remodeling links EHD1 functions to endocytic recycling. *Nat. Commun.* **9**, 5187 (2018).
49. A. Hohendahl *et al.*, Structural inhibition of dynamin-mediated membrane fission by endophilin. *Elife* **6**, e26856 (2017).
50. K. Faelber *et al.*, Crystal structure of nucleotide-free dynamin. *Nature* **477**, 556–560 (2011).
51. S. Srinivasan, V. Dharmarajan, D. K. Reed, P. R. Griffin, S. L. Schmid, Identification and function of conformational dynamics in the multidomain GTP ase dynamin. *EMBO J.* **35**, 443–457 (2016).
52. X. M. Muñoz *et al.*, Physiological impact and disease reversion for the severe form of centronuclear myopathy linked to dynamin. *JCI Insight* **5**, e137899 (2020).
53. E. M. Gibbs, A. E. Davidson, W. R. Telfer, E. L. Feldman, J. J. Dowling, The myopathy-causing mutation DNM2-S619L leads to defective tubulation *in vitro* and in developing zebrafish. *Dis. Model. Mech.* **7**, 157–161 (2013).
54. M. Meinecke *et al.*, Cooperative recruitment of dynamin and BIN/Amphiphysin/Rvs (BAR) domain-containing proteins leads to GTP-dependent membrane scission. *J. Biol. Chem.* **288**, 6651–6661 (2013).
55. E. Lemerle *et al.*, Caveolae and Bin1 form ring-shaped platforms for T-tubule initiation. *Elife* **12**, e84139 (2023).
56. R. S. Polishchuk, M. Capestrano, E. V. Polishchuk, Shaping tubular carriers for intracellular membrane transport. *FEBS Lett.* **583**, 3847–3856 (2009).
57. A. P. A. Ferreira, E. Boucrot, Mechanisms of carrier formation during clathrin-independent endocytosis. *Trends Cell Biol.* **28**, 188–200 (2018).
58. J. R. T. van Weering, P. J. Cullen, Membrane-associated cargo recycling by tubule-based endosomal sorting. *Semin. Cell Dev. Biol.* **31**, 40–47 (2014).
59. J. R. T. van Weering, P. Verkade, P. J. Cullen, SNX-BAR proteins in phosphoinositide-mediated, tubular-based endosomal sorting. *Semin. Cell Dev. Biol.* **21**, 371–380 (2010).
60. M. Chandra, B. M. Collins, The phox homology (PX) domain. *Adv. Exp. Med. Biol.* **1111**, 1–17 (2019).
61. J. Schindelin *et al.*, Fiji: An open-source platform for biological-image analysis. *Nat. Methods* **9**, 676–682 (2012).